A novel multi-radionuclide imaging method based on mechanical collimated Compton camera

Renyao Wu [a], Changran Geng [a,*], Feng Tian [a], Mingzhu Li [a], Jianfeng Xu [a,b], Fei Cai [a,b], Xiaobin Tang [a,**]

[a] *Department of Nuclear Science and Technology, Nanjing University of Aeronautics and Astronautics, Nanjing, 210016, People's Republic of China*
[b] *JYAMS PET Research and Development Limited, Nanjing, 211100, People's Republic of China*

ARTICLE INFO

ABSTRACT

Simultaneous imaging of multiple radionuclides can improve the accuracy of clinical diagnosis and therapy, and has great significance for clinical and molecular applications. However, the photon energies produced by radionuclides cover a broad energy range from a few keV to several MeV, and simultaneously imaging multiple radionuclides in such a broad energy range is a challenge. This study proposes a novel and easy-to-implement multi-radionuclide imaging method based on the mechanical collimated Compton camera (MCCC) to achieve multi-radionuclide imaging in a broad energy range. ^{18}F and ^{99m}Tc point source imaging experiments were conducted using MCCC, at a distance of 10 cm from the radioactive source, the radial full width at half maximum of ^{18}F and ^{99m}Tc point source imaging results were evaluated to be 7.3 mm and 4.5 mm. In addition, we demonstrated the feasibility of using MCCC to simultaneously imaged ^{18}F and ^{99m}Tc in mouse phantom experiments at the heart and bladder sites and the bladder and kidneys sites, the reconstructed high radioactivity area in the 3D imaging results was basically consistent with the set radioactivity distribution. Then, Monte Carlo simulations of other types of radionuclides were performed with reference to phantom experiment at the bladder and kidneys sites. Simulation results shown the promising potential of the proposed method for imaging multiple radionuclides in a broad energy range.

1. Introduction

Radionuclide imaging allows the non-invasive visualization of the location distribution of radionuclide-labeled specific radiopharmaceuticals in living organisms and is widely used in the diagnosis and therapy of several diseases (Filippou and Tsoumpas, 2018; Geng et al., 2019; Hu et al., 2022). Multi-radionuclide imaging enables the simultaneous acquisition of multiple functional imaging results in a single scan and can avoid the co-registration problems. Analyzing the relationship between several kinds functional imaging results will benefit clinical diagnosis and therapy (Adachi et al., 2016; Knight et al., 2019; Lamichhane et al., 2017; Takeuchi, 2016; Wu and Liu, 2019). Several studies that applied multi-radionuclide imaging have been reported, e.g. myocardial perfusion, brain diagnosis, and tumor hypoxia assessment (Bocher et al., 2010; Du and Frey, 2009; Kacperski et al., 2011; Lehtiö et al., 2003; O'Brien et al., 2014).

Imaging of radionuclides is accomplished by detecting the photons produced by the target radionuclide. Currently, single photon emission computed tomography (SPECT) and positron emission computed tomography (PET) are widely used for radionuclide imaging (Del Guerra and Belcari, 2007). Studies have shown that simultaneously imaging of multiple PET tracers can provide comprehensive information for disease diagnosis (Kadrmas and Hoffman, 2013; Nandhagopal et al., 2009). However, PET tracers can only use positron radionuclide-labeled radiopharmaceuticals.

Meanwhile, for multi-radionuclide SPECT imaging, several groups have reported clinical examples of cardiac imaging, brain imaging, and imaging of bone and joint infections (Berman et al., 2009; Hsieh et al., 2010; van der Bruggen et al., 2010). However, because the limitations of collimator, conventional mechanical-collimation SPECT can only image radionuclides that emit low-energy photons, typically below 300 keV (Motomura et al., 2008).

In this context, several studies have proposed the use of a Compton camera (CC) for multi-radionuclide imaging because of its wide energy detection range (hundreds keV to a few MeV) and multi-radionuclide detection capability (Kishimoto et al., 2017; Motomura et al., 2008; Nakano et al., 2020; Sakai et al., 2018b; Suzuki et al., 2013; Todd et al., 1974). For example, Suzuki et al. successfully achieved the simultaneous three-dimensional (3D) imaging of ^{64}Cu and ^{131}I in animal experiments using a Si/CdTe CC (Suzuki et al., 2013). In 2020, Nakano et al. conducted a human clinical trial of CC-based simultaneous ^{18}F and ^{99m}Tc *in-vivo* imaging (Nakano et al., 2020).

In addition, CC-based detector systems that combine multiple imaging modalities have also been proposed to perform multi-radionuclide imaging. Omata et al. introduced a hybrid CC (HCC), which combines the imaging modalities of CC and pinhole camera in a single system, and demonstrated the performance of the HCC for the simultaneous imaging of multi-radionuclide in a wide energy band (Omata et al., 2020, 2022). Several groups focused on a hybrid PET-Compton imaging system, this 2-in-1 device enables the simultaneous imaging of PET and SPECT tracers (Ogane et al., 2021; Shimazoe et al., 2020; Tashima et al., 2020; Uenomachi et al., 2021; Yoshida et al., 2020). Integrated imaging systems such as these, which combine various imaging principles, can be adapted to meet complex multi-radionuclide detection requirements. However, the photon energies produced by the radionuclides cover an energy range of a few keV to several MeV, and the simultaneous imaging of multiple radionuclides in such a broad energy spectral range is still challenging.

Combining the advantages of conventional mechanical collimation SPECT systems in detecting low-energy photons and CC in detecting high-energy photons in one imaging system, we propose a novel and easy-to-implement imaging method based on a mechanical collimated CC (MCCC) to achieve the simultaneous imaging of multiple radionuclides over a broad energy range. We established a MCCC prototype, evaluated its basic performance, performed experiments on simultaneous ^{18}F and ^{99m}Tc imaging on a mouse phantom. ^{18}F and ^{99m}Tc are clinically representative radionuclides, whose characteristic energies are 511 and 141 keV, respectively; they are suitable for verifying the simultaneous broad-energy band multi-radionuclide imaging performance of the MCCC. Further demonstrated the promising prospect of the MCCC for the simultaneous imaging of multiple radionuclides in a wide energy range through Monte Carlo (MC) simulations.

2. Materials and method

2.1. Concept of multi-radionuclide imaging method based on mechanical collimated Compton camera

Fig. 1(a) shows the detailed structure of the MCCC, which consists of a detection part, that is, a CC, and a collimation part. The CC is essentially an electronically collimated SPECT modality based on Compton

scattering kinematics (Parajuli et al., 2022). Therefore, by screening the detection data into low-energy mechanical and high-energy electronical collimation detection data, the MCCC can reconstruct the source distribution of low-energy and high-energy photons with collimator SPECT and CC modalities, respectively. Fig. 1(b) shows the acquisition modes of low-energy mechanical and high-energy electronical collimation detection data.

In radionuclide imaging, the energy of the characteristic gamma rays produced by the radionuclide is generally known. Therefore, in the case of multi-radionuclide imaging, the screening of low-energy mechanical and high-energy electronical collimation detection data is parameterized by two factors, the number of interactions and an energy threshold. Specifically, if an incident photon is recorded for only one interaction, and its deposition energy falls within the energy window of low-energy photon source, then this detection event will be screened as low-energy mechanical collimation detection data. Correspondingly, if an incident photon is recorded for two interactions, and the sum of its energy deposition falls within the energy window of high-energy photon source, then this detection event will be screened as high-energy electronical collimation detection data. The width of energy window depends on the energy resolution of the detection system. Furthermore, the MCCC takes multi-angle data measurement to realize 3D reconstruction as shown in Fig. 1(c). Under the current detection conditions, a single MCCC constitutes the detection system, and the measured object rotates around a fixed rotation axis to achieve tomographic data acquisition.

2.2. Structure of mechanical collimated Compton camera

A 3D position-sensitive $Cd_{0.9}Zn_{0.1}Te$ (CZT, density is 5.8 g/cm^3) CC fabricated by Kromek group (Huddersfield, UK) was used as the detection part of the MCCC (Tian et al., 2022). The size of the CZT crystal is $22 \times 22 \times 15$ mm^3, which is divided into 11×11 pixelated anodes with one planar cathode, and the depth of interaction was inferred by calculating the time difference between the signals of the cathode and the anode (Li et al., 2022). The intrinsic spatial resolution over the whole detection volume is $2.0 \times 2.0 \times 0.34$ mm^3. In addition, a 3D printed parallel-hole tungsten collimator was used for the collimation part of the MCCC. The holes are round with a diameter of 1.2 mm, the septum thickness is 0.8 mm and the septal height is 30 mm. The collimator's size was designed to match the CZT crystal, and each collimating round hole corresponds to an anode pixel on the CZT crystal.

2.3. Mouse phantom experiments with ^{18}F and ^{99m}Tc radionuclides

The mouse phantom radionuclide distribution imaging experiments were conducted as shown in Fig. 2. The mouse phantom was referenced from a normal 28-g male mouse, and the material of its torso is butanediol dimethacrylate ($C_{12}H_{18}O_4$, ρ:1.3 g/cm^3) (Dogdas et al., 2007). The phantom contains four organs, including brain, heart, kidneys, and
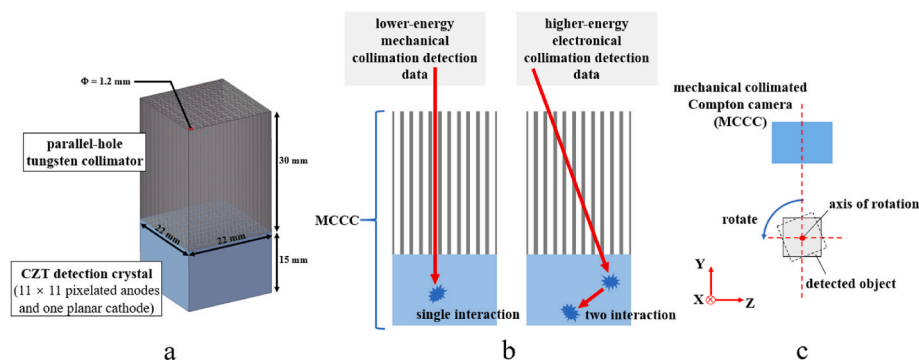

Fig. 1. Structure and imaging concept of MCCC. (a) Detailed structure of the MCCC. (b) Acquisition modes of low-energy mechanical and high-energy electronical collimation detection data. (c) Schematic of multi-angle detection of MCCC.
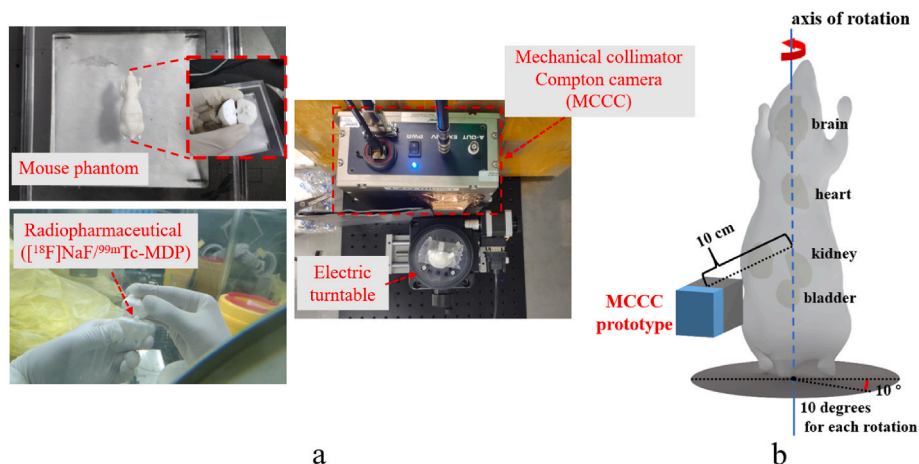
Fig. 2. Mouse phantom experiments. (a) 3D printed mouse phantom and schematic of radiopharmaceutical placement and geometry configuration of the experiments. (b) Illustration of experiment implementation.

bladder, which have been hollowed out to facilitate the placement of radiopharmaceuticals. In the experiments, a mouse phantom with organs filled with radiopharmaceuticals was placed on an electric turntable, the MCCC realized multi-angle detection through the rotation of the electric turntable. The MCCC was placed at the same height as the measured organs, facing the axis of rotation, and the surface of the CZT CC was 10 cm away from the center of rotation.

In the experiments, [^{18}F]NaF and ^{99m}Tc-MDP were encapsulated and then placed in the sites of the mouse phantom's organs. Two groups of phantom experiments were performed in this study. Referring to the radionuclide imaging study of Sakai et al., the activity concentration of ^{18}F and ^{99m}Tc in clinical examination is approximately equal (Sakai et al., 2018b). For this study, in the radionuclide imaging experiment at the heart and bladder sites, the activities of ^{18}F and ^{99m}Tc in the heart and bladder organs were ~1.6 and 1.4 MBq, which were ~7.1 and 7.2 MBq/mL in activity concentration, respectively. In the radionuclide imaging experiment at the bladder and kidneys sites, the activities of ^{18}F and ^{99m}Tc in the bladder and each kidney organs were ~2.0 and 1.8 MBq, which were ~10.2 and 8.1 MBq/mL in activity concentration, respectively. A total of 36 angles were detected in each experiment, and the detection time of each angle was 2 min. The energy threshold in the experiment was selected to be (511 ± 5) and (141 ± 2.5) keV, which correspond to high-energy electronical collimation detection data and low-energy mechanical collimation detection data, respectively.

2.4. Mouse phantom simulations with more types of radionuclides

Geant4 is a general-purpose MC simulation toolkit and has been widely used in nuclear physics, medical research, and other fields (Agostinelli et al., 2003). For the applications of simultaneous multi-radionuclide imaging in nuclear medicine, the potential of MCCC for simultaneous imaging of more types of radionuclides was investigated using Geant4 (version 10.05).

Mouse phantom simulations with the same geometry and radiation source setup were performed according to the mouse phantom radionuclide imaging experiment at the bladder and kidneys sites introduced in Section 2.3. The detection part in the simulations was modeled as the same pixel model as in reality. Four groups of radionuclides were considered in mouse phantom simulations, the types of radionuclides and the characteristic energies of gamma photons emitted by each radionuclide in the simulations are shown in Table 1. As with the experimental setup, low-energy radionuclides were placed in the kidneys, and high-energy radionuclides were placed in the bladder. Additionally, according to the energy resolution, Gaussian broadening was performed on the energy recorded in both high-energy electronical and

Table 1
Groups of radionuclides considered in the simulations and their characteristic energy for detection.

Lower energy radionuclide	Characteristic energy (keV)	Higher energy radionuclide	Characteristic energy (keV)
^{133}Xe	81	^{208}Tl	583
^{99m}Tc	141	^{18}F	511
^{111}In	245	^{212}Bi	727
^{131}I	364	^{95}Tc	766

low-energy mechanical collimation detection data in the post-processing detection data. The order of interactions within a Compton event corresponds to ground truth in simulated data, whereas in experimental data corresponds to a different criterion. And the physics module of Geant4 simulations performed in this study was G4EmPenelopePhysics.

2.5. Image reconstruction of mechanical collimated Compton camera

Low-energy mechanical collimation detection data relies on physical collimation to obtain the line of responses (LORs), and reconstruct the radiation source through the overlaying of LORs. An open-source software (i.e., QSPECT) was used for Maximum Likelihood Expectation Maximization (MLEM) iterative 3D reconstruction for the collimator SPECT modality (Loudos et al., 2010). High-energy electronical collimation detection data relies on Compton kinematics to generate a Compton cone; the position of the radiation source is limited to the cone surface. The Compton cone angle (θ) can be calculated as follows:

$$\theta = \mathrm{acos}\left(1 - \frac{m_e c^2 E_1}{E_2(E_1 + E_2)}\right), \tag{1}$$

where $m_e c^2$ is the electron rest mass, E_1 is the energy of recoil electrons, and E_2 is the energy of scattered photons. The list-mode MLEM (LM-MLEM) iterative algorithm was used for iterative 3D Compton imaging (Maxim et al., 2016). The ordering rule of Compton event pairs in experiments was assumed to be that the events with larger energy deposition are the scattering events (Shy and He, 2020), while the ordering rule in the simulation was based on the ground truth. In this study, the 3D reconstruction space was divided into $200 \times 200 \times 200$ voxels, and the volume of each cubic voxel is $1 \times 1 \times 1$ mm^3.

2.6. Image analysis and quantification

The reconstruction results is quantitatively evaluated using the following two indices: the signal-to-noise ratio (SNR), and the activity

recovery coefficient (ARC) for each radioactive organ *i* (Lee et al., 2018; Muñoz et al., 2022):

$$SNR = \frac{\mu_{ROI}}{\sigma_{Background}}, \qquad (2)$$

$$ARC_i = \frac{A_i \sum_j V_j}{V_i A_T}. \qquad (3)$$

For the calculation of SNR, μ_{ROI} represents the mean activity reconstructed in the region of interest (ROI), and $\sigma_{Background}$ represents the standard deviation of the activity reconstructed in the area excluding the ROI. For each organ with radioactivity, the ARC is defined as the ratio between the activity reconstructed in the organ position and its true activity. Where A_i and V_i are the activity reconstructed in radioactive organ *i* and its volume, and A_T is the total reconstructed activity in the whole 3D image. The reconstruction results of collimator SPECT and CC modalities are quantitatively analyzed separately.

3. Results

3.1. Basic performance of mechanical collimated Compton camera prototype

For the basic performance of MCCC prototype system, we evaluated the energy resolution, the spatial resolution, the angular resolution measurement (ARM), the intrinsic detection efficiency, and the crosstalk between 511 keV and 141 keV of interest in this study. The energy resolution was calculated from Gaussian fits. The spatial resolution of collimator SPECT and CC modalities were evaluated by point spread function (PSF) models, which are the Gaussian function and the sum of two Lorentzian functions with constant offset, respectively (Sakai et al., 2018a). The ARM was determined by voigt function. The intrinsic detection efficiency and the crosstalk between 511 keV and 141 keV were evaluated using Geant4.

For the energy resolution of the MCCC prototype system. Experiments were performed with different types of radionuclides (^{241}Am, ^{133}Ba, ^{99m}Tc, ^{18}F, ^{137}Cs) in the energy range from 60 keV to 662 keV. Finally, the energy resolution δ_E (full width at half maximum, FWHM) of the CZT detection crystal under different energies (*E*) was given as:

$$\delta_E = 0.3014 + 0.3624\sqrt{E}. \qquad (4)$$

The spatial resolution of MCCC prototype system was evaluated experimentally with single-point radiation source of ^{18}F (1.8 MBq) and ^{99m}Tc (1.6 MBq), respectively. In the point source experiments, the radiation sources were 10 cm away from the detection crystal surface of the MCCC, and the detection configurations were exactly the same as the mouse phantom experiments mentioned in Section 2.3.

Fig. 3(a) and (b) show the imaging results of the ^{18}F point source with 50 MLEM iterations under the CC modality and that of the ^{99m}Tc point source with 50 MLEM iterations under the collimator SPECT modality, respectively. Fig. 3(a) and (b) are the intermediate slices of the 3D reconstruction results, where the x-axis represents the coordinate axis perpendicular to the rotation plane. Fig. 3(c) and (d) show the radial distribution of the pixel value of the 3D reconstruction results of ^{18}F and ^{99m}Tc point source experiments against the distance from the source position, where the red dotted line represents the fitting function.

The FWHM of radial distribution of ^{18}F and ^{99m}Tc point source reconstruction results were evaluated to be 7.3 mm and 4.5 mm. The ARM is calculated as the FWHM of the angular distance distribution between the geometric scattering angle (calculated from the radiation source and the interaction positions) and the scattering angle calculated by Equation (1) (Uenomachi et al., 2021). The ARM of CC modality of the MCCC prototype system at 511 keV is $(15.9 \pm 0.33)°$.

In the simulations evaluating the intrinsic detection efficiency of MCCC prototype system, a mono-energy point source was placed at the center of the field of view (FOV) and 10 cm away from MCCC, and the evaluated energy range was from 50 to 1000 keV. Fig. 4 shows the detailed intrinsic detection efficiencies of the CC modality, collimator
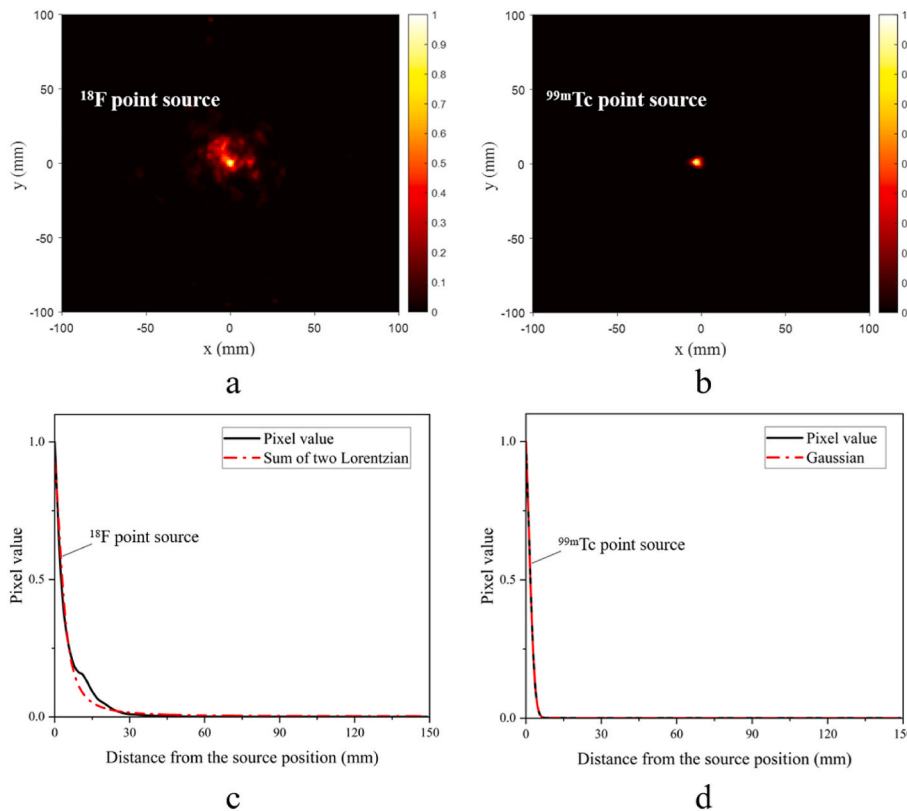

Fig. 3. Point source reconstruction results of ^{18}F and ^{99m}Tc. (a) CC imaging of ^{18}F point source. (b) Collimator SPECT imaging of ^{99m}Tc point source. (c) Radial distribution of the pixel values of the ^{18}F point source CC modality 3D imaging results (black line), and the radial distribution fitted by the sum of two Lorentzian functions (red dotted line). (d) Radial distribution of the pixel values of the ^{99m}Tc point source collimator SPECT modality 3D imaging results (black line), and the radial distribution fitted Gaussian functions (red dotted line).
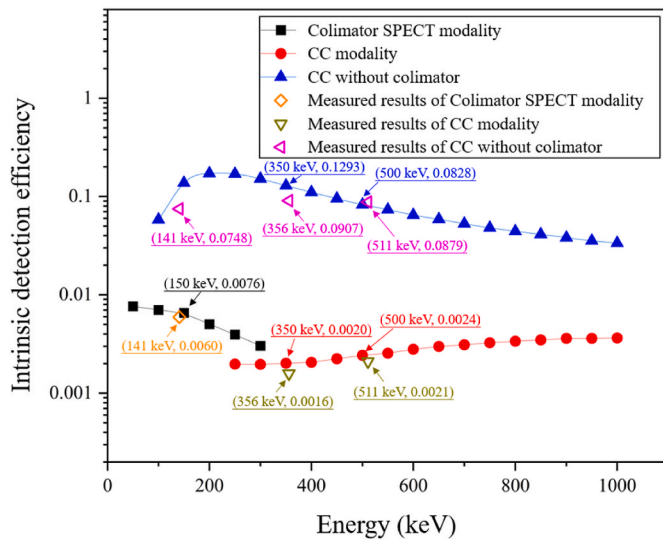
Fig. 4. Intrinsic detection efficiency of the CC modality, collimator SPECT modality, and CC without collimator as well as the measurement results for the corresponding imaging modalities.

SPECT modality, and CC without collimator. The intrinsic detection efficiency represents the proportion of detected events to all radiation emitted towards the detector, which calculated by the following equation (Omata et al., 2020):

$$\varepsilon_{int} = \frac{4\pi}{\Omega} \varepsilon_{abs}, \qquad (5)$$

where the ε_{abs} represents the absolute detection efficiency, and Ω denotes the solid angle of the detector viewed from the source.

Partial absorption events of high-energy photons can sometimes be considered as low-energy mechanical collimation detection data, a phenomenon known as crosstalk. In the simulations evaluating the crosstalk between 511 keV and 141 keV of MCCC prototype system, the 141 keV and 511 keV point sources were both placed in the center of the FOV. When the two have the same activity, 1.4% of the 141 keV low-energy mechanical collimation detection data will come from the partial absorption events of 511 keV photons.

3.2. Mouse phantom experiment results

Fig. 5 shows the 3D reconstruction results of the radiopharmaceutical distribution in the mouse phantom experiments. For the simultaneous imaging of different radionuclides through the MCCC, the imaging results of the CC and collimator SPECT modalities were normalized, respectively. Then, the normalized 3D reconstruction results of the two modalities were fused within the same coordinate system. For the radiopharmaceutical imaging experiment at the heart and bladder sites, Fig. 5(a) shows the reconstructed results and the corresponding slice layers. The accumulation of radiopharmaceuticals in the heart and the bladder is clearly visible in the reconstructed images and basically consistent with the expected distribution.

For the radiopharmaceutical imaging experiment at the bladder and kidneys sites, Fig. 5(b) shows the reconstructed results and the corresponding slice layers. Bladder and kidneys are closely adjacent organs, and the accumulation of radiopharmaceuticals in these organs is also clearly visible in the reconstructed images, which is as expected.

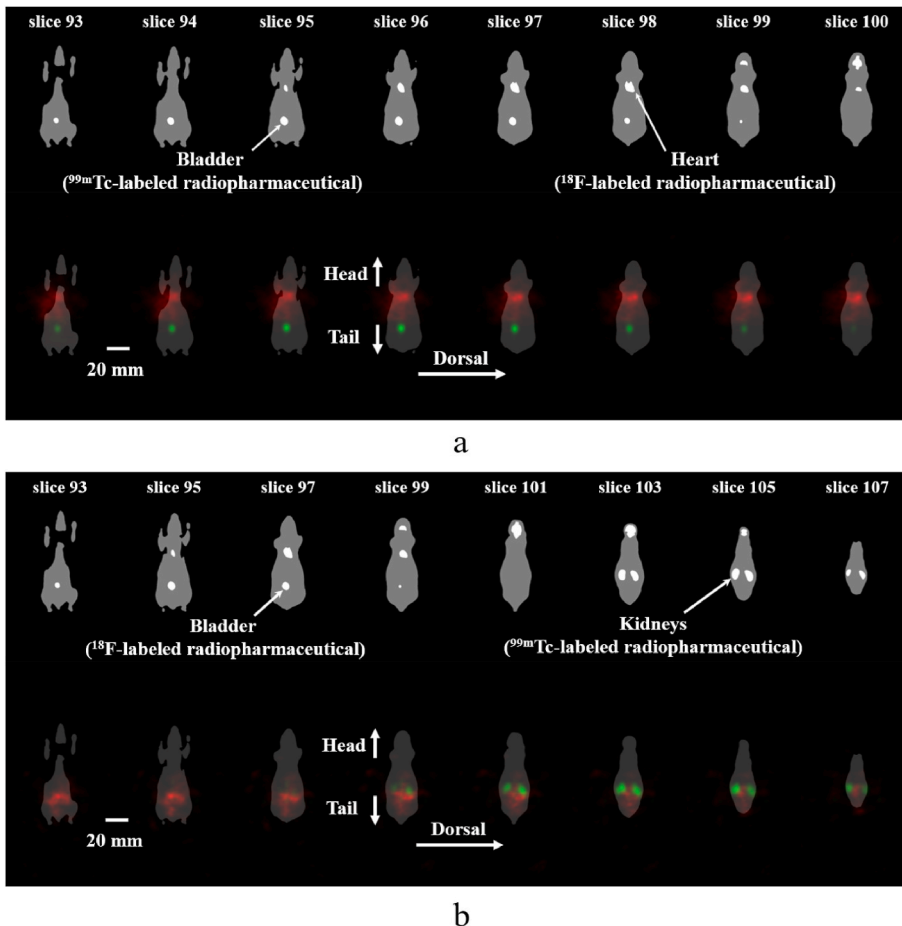Table 2 shows the quantitative analysis results of the reconstructed

Fig. 5. Reconstruction results of radiopharmaceutical distribution in the mouse phantom experiments. The red and green colors represent the reconstruction results of ^{18}F and ^{99m}Tc radiopharmaceutical distribution, respectively. The first row of each subgraph shows the phantom slices, and the second row shows the reconstruction results. (a) Reconstruction results and corresponding phantom slices in the case of radionuclide imaging experiment at the heart and bladder site, showing reconstruction results from slices 93 to 100. (b) Reconstruction results and corresponding phantom slices in the case of radionuclide imaging experiment at the bladder and kidneys site, showing reconstruction results of slices 93, 95, 97, 99, 101, 103, 105 and 107.

Table 2
SNR and ARC of the reconstructed results obtained from the experimental data.

Multi-radionuclide phantom experiment		SNR	ARC
Heart and bladder sites	CC modality	4.38	0.05
	Collimator SPECT modality	23.98	0.48
Bladder and kidneys sites	CC modality	3.87	0.05
	Collimator SPECT modality	6.36	0.32

Table 3
Detection efficiency of different groups of mouse phantom simulation.

Mouse phantom simulation	Detection efficiency of CC modality	Detection efficiency of collimator SPECT modality
^{208}TI (583 keV) and ^{133}Xe (81 keV)	4.79×10^{-5}	2.98×10^{-4}
^{18}F (511 keV) and ^{99m}Tc (141 keV)	4.08×10^{-5}	1.85×10^{-4}
^{212}Bi (727 keV) and ^{111}In (245 keV)	5.60×10^{-5}	7.49×10^{-5}
^{95}Tc (766 keV) and ^{131}I (364 keV)	5.70×10^{-5}	3.26×10^{-5}

images obtained from the mouse phantom experimental data. In the radionuclide imaging experiment at the heart and bladder sites, the ARC was associated with heart in CC modality and with bladder in collimator SPECT modality. And in the radionuclide imaging experiment at the bladder and kidneys sites, the ARC was associated with bladder in CC modality and with kidneys in collimator SPECT modality.

3.3. Potential imaging performance with radionuclides of different energies

Fig. 6 shows the reconstruction results of different groups of radionuclides, under the simulation setups of radiopharmaceutical imaging at the bladder and kidneys sites described in Section 2.4. It can be seen from Fig. 6 that for each group of radionuclide simulations, the reconstructed distribution of radiation sources with different energies is basically consistent with the set activity distribution.

Table 3 shows the detection efficiency under different groups of simulations. The detection efficiency is calculated as the ratio of the number of low-energy mechanical and high-energy electronical collimation detection events to the total number of particles produced by the corresponding radioactive source. The change trend of the detection efficiency of the MCCC at different energies is the same as that in Fig. 4. Correspondingly, in the phantom experiments at bladder and kidneys sites using ^{18}F and ^{99m}Tc radiopharmaceuticals, the detection

efficiencies of the CC and collimator SPECT modalities are 3.40×10^{-5} and 1.51×10^{-4}, respectively.

Fig. 7 shows the quantitative analysis of the reconstruction results obtained from the phantom simulations and the comparison with phantom experiment at the bladder and kidneys sites. The SNR and ARC of the collimator SPECT modality decrease significantly as the energy of low-energy radionuclides increased, while those of the CC modality are almost constant with the change of the energy of the high-energy radionuclides. In addition, Fig. 7 shows that the evaluation values of SNR and ARC of CC and collimator SPECT modalities obtained from phantom experiment at the bladder and kidneys sites are less than the corresponding phantom simulation.

4. Discussion

This study proposes a novel MCCC-based multi-radionuclide imaging method. The developed MCCC prototype is a detection system consisting of a single-layer CZT CC and a mechanical collimator. We further show the promising application of this method against the challenge of multi-radionuclide imaging over a broad energy range, indicating that a wide
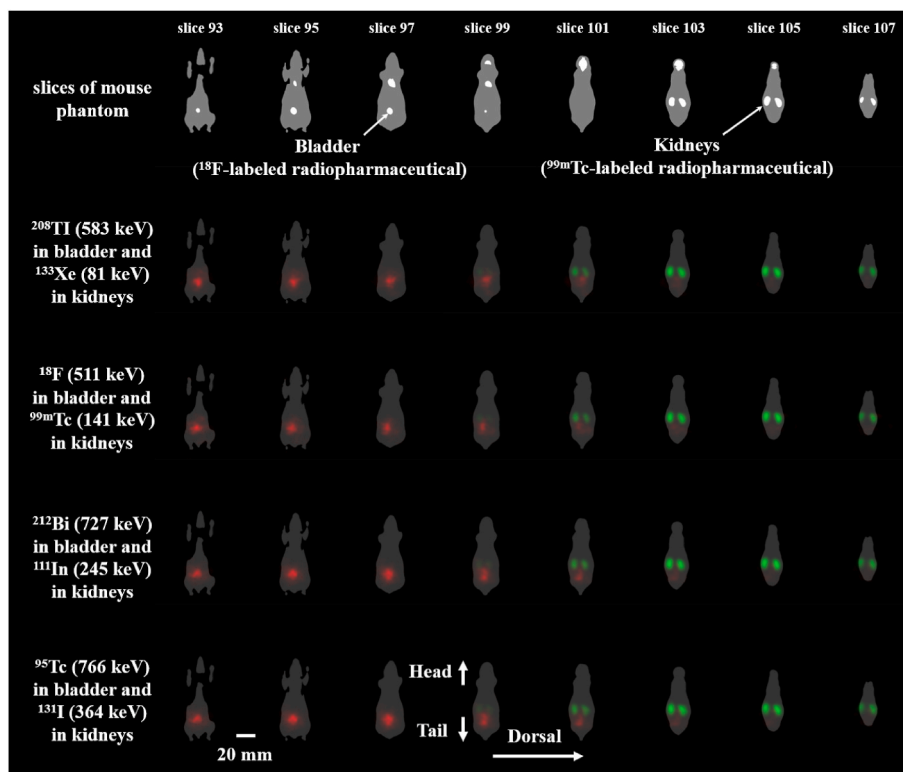

Fig. 6. Reconstruction results of mouse phantom of different groups of radionuclides in mouse phantom simulations. The red and green colors represent the reconstruction results of high-energy and low-energy radionuclides distribution, respectively, showing reconstruction results of slices 93, 95, 97, 99, 101, 103, 105 and 107.
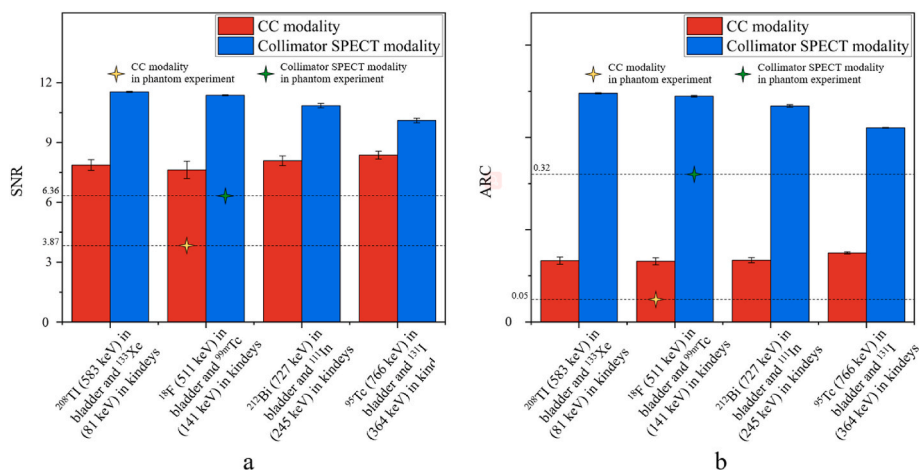
Fig. 7. Quantitative evaluation of mouse phantom reconstruction results obtained by phantom simulations and phantom experiment at the bladder and kidneys sites. (a) SNR analysis of reconstructed images obtained by phantom simulations and phantom experiment. (b) ARC analysis of reconstructed images obtained by phantom simulations and phantom experiment.

variety of radionuclides can be used. The expansion of the available radionuclide species can potentially reduce the cost of production of radiopharmaceuticals, which are currently routinely produced at each medical center's cyclotron facility, and provide opportunities for wide applications (Kishimoto et al., 2017; Sakai et al., 2018b).

The basic imaging performance of the developed MCCC prototype is shown in Fig. 3. The MCCC demonstrated spatial resolutions of approximately 7.3 and 4.5 mm for ^{18}F and ^{99m}Tc in the point source experiments, respectively. The radionuclide will decay spontaneously. In order to make the counting at each detection angle even in the experiments, this study adopted the method of reversing measurement, that is, turn forward one circle (detection at intervals of 10° for 1 min) and then reverse one circle (detection at intervals of 10° for 1 min). In the future, in a real ring detector system, the radionuclide detection will actually only take a few minutes, in this case there is no need for reversing measurement, and image quality deterioration caused by spontaneous decay can be avoided.

In Fig. 3, obvious artifacts can be observed in the imaging results of the CC modality, which are also reflected in the imaging results of radionuclides in the phantom. This phenomenon occurred because the energy and spatial resolutions of the detector and Doppler broadening led to errors in the half-apex angle of the Compton cone and thus resulted in an incorrect estimate of the source distribution. Some methods for modeling the errors of the half-apex angle in the CC reconstruction algorithms have been reported, providing a reference for future work (Andreyev et al., 2016; Ida et al., 2019; Yao et al., 2019).

Fig. 4 shows the intrinsic detection efficiency distribution of MCCC at different energies. As the energy of low-energy photon increases, the probability of the photoelectric effect decreases, so the detection efficiency of the collimator SPECT modality also decreases. As the energy of high-energy photon increases, the attenuation effect of the collimator decreases, so the detection efficiency of the CC modality increases accordingly. In the absence of the collimator, as the energy of the incident photon increases, the probability of the photon transmission out of the detector increases, resulting in a decrease in detection efficiency.

The existence of the collimator will inhibit the detection efficiency of the CC. Since detection efficiency is only one of the parameters related to image reconstruction, it may not be positively correlated with image quality. We conducted a preliminary experiment to illustrate this, and details are given in Appendix 1. At the same time, we analyzed that in the case that the 141 keV and 511 keV point sources located at the center of the FOV having the same activity, the miscount of 141 keV low-energy mechanical collimation detection data generated by 511 keV photons only accounts for 1.4% of the total low-energy mechanical collimation

detection data. Therefore, the crosstalk was not studied here.

Through the phantom experiments, we successfully demonstrated the simultaneous *in-vivo* imaging of ^{18}F and ^{99m}Tc labeled radiopharmaceuticals using the MCCC-based multi-radionuclide imaging method. As shown in Fig. 5, the reconstruction results of both two phantom experiments are consistent with the set high radioactivity areas. Previous studies revealed that relatively high Compton cross sections can be achieved in the low-energy range with Si detectors as scatterers in CCs (Watanabe et al., 2005). Studies on the simultaneous *in-vivo* imaging of ^{18}F and ^{99m}Tc have been performed by other groups using a multi-layer Si/CdTe CC before, but these studies still show limitations in the detection efficiency and angular resolution for 141-keV gamma rays (Nakano et al., 2020; Sakai et al., 2018b).

The proposed MCCC has a simpler structure than the multi-layer Si/CdTe CC and can achieve accurate *in-vivo* 3D imaging of 141 keV gamma rays through the collimator SPECT modality. The activity ratio of ^{18}F and ^{99m}Tc radiopharmaceuticals in current phantom experiments was approximately equal to 1, and more phantom experiments with different activity ratios can be carried out in the future to study the relationship between the imaging results and different activity ratios.

Through MC simulations, we further demonstrated the imaging results of the simultaneous *in-vivo* imaging of other types of radionuclides in a broad energy range, from 81 keV to 766 keV. The types of radionuclides considered in the simulations contained radionuclides used in diagnosis and therapy. The evaluated values of ARC in CC and collimator SPECT modalities from the phantom simulations were comparable to those in previous reports (Muñoz et al., 2022; van der Velden et al., 2019). The results of the quantitative evaluation show that the current MCCC structure can accommodate multi-radionuclide imaging with more characteristic energy nuclides.

Uncertainties in energies and interaction locations are considered in the simulations, but we still find that the mouse phantom experimental imaging results are inferior to the simulation imaging results. The reasons may be electronic noise and the influence of neighboring pixels, etc., which are difficult to be taken into account in simulations. In addition, the ordering rule of Compton event pairs used in experiments is also one of the reasons for deteriorating the image quality of the CC modality in the reconstruction results. The current CC cannot distinguish the types of scattering and absorption interactions in a Compton event pairs. This study identifies the type of interaction events based on energy deposition, but, this method will cause a certain amount of Compton event pairs to be misordered and thus generate artifacts in reconstructed images.

Subsequent research can use sub-pixel technology to eliminate the

influence of adjacent pixels and improve the three-dimensional position resolution ability of CZT. Machine learning-based event type recognition method can also be adopted to improve the reconstructed image quality of CC modality (Kozani and Magiera, 2022; Wang et al., 2022).

At present, this study has limitations. The radioactive source settings of the current phantom experiment are relatively simple, and subsequent multi-radionuclide *in-vivo* imaging of animals is necessary for the preclinical validation. Our ultimate aim is to successfully conduct human clinical trials. Considering the increased detector distance from the measured object and volume effects in this case, the optimized reconstruction algorithm and the detector settings must be considered. The volume of the current detection crystal is very small, that is, only 22 $\times$ 22 $\times$ 15 mm^3. The use of the CZT array will effectively expand the reconstruction space of the collimator SPECT modality and the imaging effect of the CC modality.

5. Conclusion

In this study, we propose a MCCC-based multi-radionuclide imaging method. With this method, we demonstrated the simultaneous *in-vivo* imaging results of the ^{99m}Tc and ^{18}F obtained from the phantom experimental detection data of the heart and bladder sites and the bladder and kidneys sites. The evaluation values of activity recovery coefficients of CC and collimator SPECT modalities obtained in the phantom experiment at the heart and bladder sites were 0.05 and 0.48, and that in the phantom experiment at the bladder and kidneys sites were 0.05 and 0.32. Further, through Monte Carlo simulations with an ideal ordering rule, the proposed method showed a promising capability to image other types of radionuclides in a wide energy range. These results demonstrate the promising application of the proposed methodology.

Declaration of competing interest

The authors declare that they have no known competing financial interests or personal relationships that could have appeared to influence the work reported in this paper.

Data availability

Data will be made available on request.

Acknowledgments

Appendix A. Supplementary data

Supplementary data to this article can be found online at https://doi.org/10.1016/j.radmeas.2023.106938.

References

Adachi, N., Yoshii, Y., Furukawa, T., Yoshimoto, M., Takeuchi, Y., Inubushi, M., Wakizaka, H., Tsuji, A.B., Takahashi, M., Fujibayashi, Y., Saga, T., 2016. In vivo simultaneous imaging of vascular pool and hypoxia with a HT-29 tumor model: the application of dual-isotope SPECT/PET/CT. Intermt. J. Sci. 25, 26–39, 2016.

Agostinelli, S., Allison, J., Amako, K., Apostolakis, J., Araujo, H., Arce, P., Asai, M., Axen, D., Banerjee, S., Barrand, G., Behner, F., Bellagamba, L., Boudreau, J., Broglia, L., Brunengo, A., Burkhardt, H., Chauvie, S., Chuma, J., Chytracek, R., Cooperman, G., Cosmo, G., Degtyarenko, P., Dell'Acqua, A., Depaola, G., Dietrich, D., Enami, R., Feliciello, A., Ferguson, C., Fesefeldt, H., Folger, G., Foppiano, F., Forti, A., Garelli, S., Giani, S., Giannitrapani, R., Gibin, D., Gómez

Cadenas, J.J., González, I., Gracia Abril, G., Greeniaus, G., Greiner, W., Grichine, V., Grossheim, A., Guatelli, S., Gumplinger, P., Hamatsu, R., Hashimoto, K., Hasui, H., Heikkinen, A., Howard, A., Ivanchenko, V., Johnson, A., Jones, F.W., Kallenbach, J., Kanaya, N., Kawabata, M., Kawabata, Y., Kawaguti, M., Kelner, S., Kent, P., Kimura, A., Kodama, T., Kokoulin, R., Kossov, M., Kurashige, H., Lamanna, E., Lampén, T., Lara, V., Lefebure, V., Lei, F., Liendl, M., Lockman, W., Longo, F., Magni, S., Maire, M., Medernach, E., Minamimoto, K., Mora de Freitas, P., Morita, Y., Murakami, K., Nagamatu, M., Nartallo, R., Nieminen, P., Nishimura, T., Ohtsubo, K., Okamura, M., O'Neale, S., Oohata, Y., Paech, K., Perl, J., Pfeiffer, A., Pia, M.G., Ranjard, F., Rybin, A., Sadilov, S., Di Salvo, E., Santin, G., Sasaki, T., Savvas, N., Sawada, Y., Scherer, S., Sei, S., Sirotenko, V., Smith, D., Starkov, N., Stoecker, H., Sulkimo, J., Takahata, M., Tanaka, S., Tcherniaev, E., Safai Tehrani, E., Tropeano, M., Truscott, P., Uno, H., Urban, L., Urban, P., Verderi, M., Walkden, A., Wander, W., Weber, H., Wellisch, J.P., Wenaus, T., Williams, D.C., Wright, D., Yamada, T., Yoshida, H., Zschiesche, D., 2003. Geant4—a simulation toolkit. Nucl. Instrum. Methods Phys. Res. Sect. A Accel. Spectrom. Detect. Assoc. Equip. 506, 250–303. https://doi.org/10.1016/S0168-9002(03)01368-8.

Andreyev, A., Celler, A., Ozsahin, I., Sitek, A., 2016. Resolution recovery for Compton camera using origin ensemble algorithm: resolution recovery for Compton camera. Med. Phys. 43, 4866–4876. https://doi.org/10.1118/1.4959551.

Berman, D.S., Kang, X., Tamarappoo, B., Wolak, A., Hayes, S.W., Nakazato, R., Thomson, L.E.J., Kite, F., Cohen, I., Slomka, P.J., Einstein, A.J., Friedman, J.D., 2009. Stress thallium-201/rest technetium-99m sequential dual isotope high-speed myocardial perfusion imaging. JACC: Cardiovasc. Imag. 2, 273–282. https://doi.org/10.1016/j.jcmg.2008.12.012.

Bocher, M., Blevis, I.M., Tsukerman, L., Shrem, Y., Kovalski, G., Volokh, L., 2010. A fast cardiac gamma camera with dynamic SPECT capabilities: design, system validation and future potential. Eur. J. Nucl. Med. Mol. Imag. 37, 1887–1902. https://doi.org/10.1007/s00259-010-1488-z.

Del Guerra, A., Belcari, N., 2007. State-of-the-art of PET, SPECT and CT for small animal imaging. Nucl. Instrum. Methods Phys. Res. Sect. A Accel. Spectrom. Detect. Assoc. Equip. 583, 119–124. https://doi.org/10.1016/j.nima.2007.08.187.

Dogdas, B., Stout, D., Chatziioannou, A.F., Leahy, R.M., 2007. Digimouse: a 3D whole body mouse atlas from CT and cryosection data. Phys. Med. Biol. 52, 577–587. https://doi.org/10.1088/0031-9155/52/3/003.

Du, Y., Frey, E.C., 2009. Quantitative evaluation of simultaneous reconstruction with model-based crosstalk compensation for T99mc/I123 dual-isotope simultaneous acquisition brain SPECT: quantitative dual-isotope brain SPECT. Med. Phys. 36, 2021–2033. https://doi.org/10.1118/1.3120411.

Filippou, V., Tsoumpas, C., 2018. Recent advances on the development of phantoms using 3D printing for imaging with CT, MRI, PET, SPECT, and ultrasound. Med. Phys. 45, e740–e760. https://doi.org/10.1002/mp.13058.

Geng, C.-R., Ai, Y., Tang, X.-B., Shu, D.-Y., Gong, C.-H., Du, M.-H., Ji, F.-Q., 2019. Quantum dots enhanced Cerenkov luminescence imaging. Nucl. Sci. Tech. 30, 71. https://doi.org/10.1007/s41365-019-0599-x.

Hsieh, P.C., Lee, I.H., Yeh, T.L., Chen, K.C., Huang, H.C., Chen, P.S., Yang, Y.K., Yao, W. J., Lu, R.-B., Chiu, N.T., 2010. Distribution volume ratio of serotonin and dopamine transporters in euthymic patients with a history of major depression — a dual-isotope SPECT study. Psychiatr. Res. Neuroimaging 184, 157–161. https://doi.org/10.1016/j.pscychresns.2010.09.004.

Hu, X., Li, D., Fu, Y., Zheng, J., Feng, Z., Cai, J., Wang, P., 2022. Advances in the application of radionuclide-labeled HER2 affibody for the diagnosis and treatment of ovarian cancer. Front. Oncol. 12, 917439 https://doi.org/10.3389/fonc.2022.917439.

Ida, T., Motomura, S., Ueda, M., Watanabe, Y., Enomoto, S., 2019. Accurate modeling of event-by-event backprojection for a germanium semiconductor Compton camera for system response evaluation in the LM-ML-EM image reconstruction method. Jpn. J. Appl. Phys. 58, 016002 https://doi.org/10.7567/1347-4065/aae8e9.

Kacperski, K., Erlandsson, K., Ben-Haim, S., Hutton, B.F., 2011. Iterative deconvolution of simultaneous ^{99m}Tc and ^{201}Tl projection data measured on a CdZnTe-based cardiac SPECT scanner. Phys. Med. Biol. 56, 1397–1414. https://doi.org/10.1088/0031-9155/56/5/012.

Kadrmas, D.J., Hoffman, J.M., 2013. Methodology for quantitative rapid multi-tracer PET tumor characterizations. Theranostics 3, 757–773. https://doi.org/10.7150/thno.5201.

Kishimoto, A., Kataoka, J., Taya, T., Tagawa, L., Mochizuki, S., Ohsuka, S., Nagao, Y., Kurita, K., Yamaguchi, M., Kawachi, N., Matsunaga, K., Ikeda, H., Shimosegawa, E., Hatazawa, J., 2017. First demonstration of multi-color 3-D in vivo imaging using ultra-compact Compton camera. Sci. Rep. 7, 2110. https://doi.org/10.1038/s41598-017-02377-w.

Knight, J.C., Mosley, M.J., Kersemans, V., Dias, G.M., Allen, P.D., Smart, S., Cornelissen, B., 2019. Dual-isotope imaging allows in vivo immunohistochemistry using radiolabelled antibodies in tumours. Nucl. Med. Biol. 70, 14–22. https://doi.org/10.1016/j.nucmedbio.2019.01.010.

Kozani, M.K., Magiera, A., 2022. Machine learning-based event recognition in SiFi Compton camera imaging for proton therapy monitoring. Phys. Med. Biol. 67, 155012 https://doi.org/10.1088/1361-6560/ac71f2.

Lamichhane, N., Dewkar, G., Sundaresan, G., Mahon, R., Zweit, J., 2017. [18F]-Fluorinated carboplatin and [111In]-Liposome for image-guided drug delivery. IJMS 18, 1079. https://doi.org/10.3390/ijms18051079.

Lee, T., Kim, Y., Lee, W., 2018. High-performance Compton SPECT using both photoelectric and Compton scattering events. J. Kor. Phys. Soc. 73, 1393–1398. https://doi.org/10.3938/jkps.73.1393.

Lehtiö, K., Oikonen, V., Nyman, S., Grönroos, T., Roivainen, A., Eskola, O., Minn, H., 2003. Quantifying tumour hypoxia with fluorine-18 fluoroerythronitroimidazole

([18F] FETNIM) and PET using the tumour to plasma ratio. Eur. J. Nucl. Med. Mol. Imag. 30, 101–108.

Li, Y., Gong, P., Tang, X., Hu, Z., Wang, P., Tian, F., Wu, S., Ye, M., Zhou, C., Zhu, X., 2022. DOI correction for gamma ray energy reconstruction based on energy segment in 3D position-sensitive CdZnTe detectors. J. Inst. Met. 17, T03004 https://doi.org/10.1088/1748-0221/17/03/T03004.

Loudos, G.K., Papadimitroulas, P., Zotos, P., Tsougos, I., Georgoulias, P., 2010. Development and evaluation of QSPECT open-source software for the iterative reconstruction of SPECT images. Nucl. Med. Commun. 31, 558–566. https://doi.org/10.1097/MNM.0b013e32833841e8.

Maxim, V., Lojacono, X., Hilaire, E., Krimmer, J., Testa, E., Dauvergne, D., Magnin, I., Prost, R., 2016. Probabilistic models and numerical calculation of system matrix and sensitivity in list-mode MLEM 3D reconstruction of Compton camera images. Phys. Med. Biol. 61, 243–264. https://doi.org/10.1088/0031-9155/61/1/243.

Motomura, S., Kanayama, Y., Haba, H., Watanabe, Y., Enomoto, S., 2008. Multiple molecular simultaneous imaging in a live mouse using semiconductor Compton camera. J. Anal. At. Spectrom. 23, 1089. https://doi.org/10.1039/b802964d.

Muñoz, E., Etxebeste, A., Dauvergne, D., Létang, J.M., Sarrut, D., Maxim, V., Testa, E., 2022. Imaging of polychromatic sources through Compton spectral reconstruction. Phys. Med. Biol. 67, 195017.

Nakano, T., Sakai, M., Torikai, K., Suzuki, Y., Takeda, S., Noda, S., Yamaguchi, M., Nagao, Y., Kikuchi, M., Odaka, H., Kamiya, T., Kawachi, N., Watanabe, S., Arakawa, K., Takahashi, T., 2020. Imaging of 99m Tc-DMSA and 18 F-FDG in humans using a Si/CdTe Compton camera. Phys. Med. Biol. 65, 05LT01 https://doi.org/10.1088/1361-6560/ab33d8.

Nandhagopal, R., Kuramoto, L., Schulzer, M., Mak, E., Cragg, J., Lee, C.S., McKenzie, J., McCormick, S., Samii, A., Troiano, A., Ruth, T.J., Sossi, V., de la Fuente-Fernandez, R., Calne, D.B., Stoessl, A.J., 2009. Longitudinal progression of sporadic Parkinson's disease: a multi-tracer positron emission tomography study. Brain 132, 2970–2979. https://doi.org/10.1093/brain/awp209.

O'Brien, J.T., Firbank, M.J., Davison, C., Barnett, N., Bamford, C., Donaldson, C., Olsen, K., Herholz, K., Williams, D., Lloyd, J., 2014. 18 F-FDG PET and perfusion SPECT in the diagnosis of alzheimer and lewy body dementias. J. Nucl. Med. 55, 1959–1965. https://doi.org/10.2967/jnumed.114.143347.

Ogane, K., Uenomachi, M., Shimazoe, K., Takahashi, H., Seto, Y., Momose, T., 2021. Simultaneous measurements of single gamma ray of 131I and annihilation radiation of 18F with Compton PET hybrid camera. Appl. Radiat. Isot. 176, 109864 https://doi.org/10.1016/j.apradiso.2021.109864.

Omata, A., Kataoka, J., Fujieda, K., Sato, S., Kuriyama, E., Kato, H., Toyoshima, A., Teramoto, T., Ooe, K., Liu, Y., Matsunaga, K., Kamiya, T., Watabe, T., Shimosegawa, E., Hatazawa, J., 2020. Performance demonstration of a hybrid Compton camera with an active pinhole for wide-band X-ray and gamma-ray imaging. Sci. Rep. 10, 14064 https://doi.org/10.1038/s41598-020-71019-5.

Omata, A., Masubuchi, M., Koshikawa, N., Kataoka, J., Kato, H., Toyoshima, A., Teramoto, T., Ooe, K., Liu, Y., Matsunaga, K., Kamiya, T., Watabe, T., Shimosegawa, E., Hatazawa, J., 2022. Multi-modal 3D imaging of radionuclides using multiple hybrid Compton cameras. Sci. Rep. 12, 2546. https://doi.org/10.1038/s41598-022-06401-6.

Parajuli, R.K., Sakai, M., Parajuli, R., Tashiro, M., 2022. Development and Applications of Compton Camera—A Review.

Sakai, M., Parajuli, R.K., Kikuchi, M., Yamaguchi, M., Nagao, Y., Kawachi, N., Arakawa, K., Nakano, T., 2018a. Effect of number of views on cross-sectional Compton imaging: a fundamental study with backprojection. Phys. Med. 56, 1–9. https://doi.org/10.1016/j.ejmp.2018.11.006.

Sakai, M., Yamaguchi, M., Nagao, Y., Kawachi, N., Kikuchi, M., Torikai, K., Kamiya, T., Takeda, S., Watanabe, S., Takahashi, T., Arakawa, K., Nakano, T., 2018b. *In vivo*

simultaneous imaging with 99m Tc and 18 F using a Compton camera. Phys. Med. Biol. 63, 205006 https://doi.org/10.1088/1361-6560/aae1d1.

Shimazoe, K., Yoshino, M., Ohshima, Y., Uenomachi, M., Oogane, K., Orita, T., Takahashi, H., Kamada, K., Yoshikawa, A., Takahashi, M., 2020. Development of simultaneous PET and Compton imaging using GAGG-SiPM based pixel detectors. Nucl. Instrum. Methods Phys. Res. Sect. A Accel. Spectrom. Detect. Assoc. Equip. 954, 161499 https://doi.org/10.1016/j.nima.2018.10.177.

Shy, D., He, Z., 2020. Gamma-ray tracking for high energy gamma-ray imaging in pixelated CdZnTe. Nucl. Instrum. Methods Phys. Res. Sect. A Accel. Spectrom. Detect. Assoc. Equip. 954, 161443 https://doi.org/10.1016/j.nima.2018.10.121.

Suzuki, Y., Yamaguchi, M., Odaka, H., Shimada, H., Yoshida, Y., Torikai, K., Satoh, T., Arakawa, K., Kawachi, N., Watanabe, Shigeki, Takeda, S., Ishikawa, S., Aono, H., Watanabe, Shin, Takahashi, T., Nakano, T., 2013. Three-dimensional and multienergy gamma-ray simultaneous imaging by using a Si/CdTe Compton camera. Radiology 267, 941–947. https://doi.org/10.1148/radiol.13121194.

Takeuchi, W., 2016. Simultaneous Tc-99m and I-123 Dual-Radionuclide Imaging with a Solid-State Detector-Based Brain-SPECT System and Energy-Based Scatter Correction, vol. 18.

Tashima, H., Yoshida, E., Wakizaka, H., Takahashi, M., Nagatsu, K., Tsuji, A.B., Kamada, K., Parodi, K., Yamaya, T., 2020. 3D Compton image reconstruction method for whole gamma imaging. Phys. Med. Biol. 65, 225038 https://doi.org/10.1088/1361-6560/abb92e.

Tian, F., Geng, C., Yao, Z., Wu, R., Xu, J., Cai, F., Tang, X., 2022. Radiopharmaceutical imaging based on 3D-CZT Compton camera with 3D-printed mouse phantom. Phys. Med. 96, 140–148. https://doi.org/10.1016/j.ejmp.2022.03.005.

Todd, R., Nightingale, J., Everett, D., 1974. A proposed γ camera. Nature 251, 132–134.

Uenomachi, M., Takahashi, M., Shimazoe, K., Takahashi, H., Kamada, K., Orita, T., Ogane, K., Tsuji, A.B., 2021. Simultaneous in vivo imaging with PET and SPECT tracers using a Compton-PET hybrid camera. Sci. Rep. 11, 17933 https://doi.org/10.1038/s41598-021-97302-7.

van der Bruggen, W., Bleeker-Rovers, C.P., Boerman, O.C., Gotthardt, M., Oyen, W.J.G., 2010. PET and SPECT in osteomyelitis and prosthetic bone and joint infections: a systematic review. Semin. Nucl. Med. 40, 3–15. https://doi.org/10.1053/j.semnuclmed.2009.08.005.

van der Velden, S., Dietze, M.M., Viergever, M.A., de Jong, H.W., 2019. Fast technetium-99m liver SPECT for evaluation of the pretreatment procedure for radioembolization dosimetry. Med. Phys. 46, 345–355.

Wang, C., Wei, L., Zhang, Z., Li, D., Feng, B., Liu, Y., Xiang, Y., Li, X., Jiang, X., 2022. Achieving sub-pixel position resolution and sub-millimeter depth resolution using a pixelated CdZnTe detector. Nucl. Instrum. Methods Phys. Res. Sect. A Accel. Spectrom. Detect. Assoc. Equip. 1033, 166685 https://doi.org/10.1016/j.nima.2022.166685.

Watanabe, S., Tanaka, T., Nakazawa, K., Mitani, T., Oonuki, K., Takahashi, T., Takashima, T., Tajima, H., Fukazawa, Y., Nomachi, M., Kubo, S., Onishi, M., Kuroda, Y., 2005. A Si/CdTe semiconductor Compton camera. IEEE Trans. Nucl. Sci. 52, 2045–2051. https://doi.org/10.1109/TNS.2005.856995.

Wu, J., Liu, C., 2019. Recent advances in cardiac SPECT instrumentation and imaging methods. Phys. Med. Biol. 64, 06TR01 https://doi.org/10.1088/1361-6560/ab04de.

Yao, Z., Xiao, Y., Chen, Z., Wang, B., Hou, Q., 2019. Compton-based prompt gamma imaging using ordered origin ensemble algorithm with resolution recovery in proton therapy. Sci. Rep. 9, 1133. https://doi.org/10.1038/s41598-018-37623-2.

Yoshida, E., Tashima, H., Nagatsu, K., Tsuji, A.B., Kamada, K., Parodi, K., Yamaya, T., 2020. Whole gamma imaging: a new concept of PET combined with Compton imaging. Phys. Med. Biol. 65, 125013 https://doi.org/10.1088/1361-6560/ab8e89.